Supporting Information

for "Cryo-Electron Tomography Reveals the Sequential Assembly of Bacterial Flagella in *Borrelia burgdorferi*" by Xiaowei Zhao, Kai Zhang, Tristan Boquoi, Bo Hu, Md A. Motaleb, Kelly A. Miller, Milinda E. James, Nyles W. Charon, Michael D. Manson, Steven J. Norris, Chunhao Li, and Jun Liu

Bacterial strains and growth conditions. High-passage avirulent *Borrelia burgdorferi sensu stricto* strain B31A (wild type) and its isogenic mutants (Table S1) were grown in BSK-II liquid medium supplemented with 6% rabbit serum or on semi-solid agar plates at 34 °C in the presence of 3-5 % carbon dioxide as previously described (1).

Constructing vectors for the targeted mutagenesis of *flgB*, *flgC*, *fliE*, *flgE*, *flhO* and *flgG* gene. Genes *flgB* [*bb0294*], *flgC* [*bb0293*], *fliE* [*bb0292*], and *flgE* [*bb0283*] are located in the *flgB* operon (Fig. S4), consisting of approximately 26 motility genes (2); *flhO* [*bb0775*, a homolog of FlgF] and *flgG* [*bb0774*] are located within the *flhO* motility gene operon (1). These genes are transcribed as polycistronic mRNA. Thus, insertion of an antibiotic resistance cassette may have a polar effect on their downstream gene expression. To avoid potential polar effect on a downstream gene expression, our recently reported gene replacement *in-frame* deletion method (3) was used to construct the targeted mutagenesis in *flgB, flgC, flgBC* (deleting both *flgB* and *flgC*)*, fliE, flgE* and *flhO* genes. As illustrated in Fig. S6, the entire open reading frames (*orfs*) of these genes were *in-frame* deleted and replaced with either a kanamycin resistance marker (*aphI*) or a spectinomycin/streptomycin resistance marker (*aadA*). A previously described targeted mutagenesis method (4) was used to construct the vector for inactivation of *flgG* by directly inserting the *aphI* cassette at a ClaI restriction enzyme cut site within the gene. The resulting constructs were designated as *flgB::aphI*, *flgC::aphI*, *flgBC::aphI*, *fliE::aadA*, *flgE::aphI*, *flhO::aphI*, and *flgG::aphI* (Fig. S6). The PCR primers for constructing these vectors are listed in Table S5.

Isolations of *flgB*, *flgC*, *flgBC*, *fliE*, *flgE*, *flhO* and *flgG* mutants. To inactivate these genes, the above constructed vectors were first linearized and then separately transformed into B31A competent cells via electroporation as previously reported (5). Transformants were selected on BSK-II agar plates containing kanamycin (350 μg ml^{-1}) or streptomycin (80 μg ml^{-1}). A previously described PCR method (4, 6) was used to determine if these genes were targeted by the resistance cassettes as expected. For each targeted gene, three primers were designed: one primer at the flanking region of a construct (e.g., *flgB::aphI*), one at its downstream end, and the third one at the 3'end of *aphI* or *aadA*. For example, for the characterization of *flgB* mutant clones, the primer P1, P7, and P23 were used in the PCR analyses. Detection of a 2.9 kb PCR product by P1/P7 and a 1.4 kb product by P1/P23 indicated that the *flgB* gene is deleted and replaced by the *aphI* cassette as expected. A similar scenario as *flgB* mutation occurred in the analysis of other six mutants by PCR (Fig. S7), indicating that these genes were mutated as expected. To confirm the *fliE* mutant, PCR was performed using the P37 and P42 primers and the resulting products were 1.9 kb for wild type and 2.4 kb for the mutants (Fig. S7). The resulting mutants were named: Δ*flgB*, Δ*flgC*, Δ*flgBC*, Δ*flgC* Δ*fliE,* Δ*flgE,* Δ*flhO*, and Δ*flgG*.

Complementation of the *flgE* mutant. For the complementation of the Δ*flgE* mutant, a *cis*-complementation approach was used by inserting the entire *flgE* gene together with its native promoter (P_{flgB}) into the intergenic region between *bb0445* and *bb0446* (7) at the BamHI cut site as shown in Fig. S8. The complementation vector, pFlgE/cis, was linearized with ApaI and electro-transformed into Δ*flgE* competent cells. PCR analysis showed that pFlgE/cis was inserted into the intergenic region

between *bb0445* and *bb0446* on the chromosome of Δ*flgE* as expected (Fig. S8). Immunoblotting analysis showed that the expression of *flgE* was restored in Δ$flgE^{com}$, a complemented clone (Fig. S8).

Periplasmic flagella (PFs) purification. The purified PFs were prepared as described previously with minor modifications (6). Approximately 250 ml of late-logarithmic-phase cells (1.5×10^8 cells/ml) were centrifuged at 8,000 × g for 20 min, washed in 10 ml of 150 mM phosphate-buffered saline (pH 7.4) (PBS), and centrifuged at 8,000 × g for 10 min at room temperature. The cell pellet was resuspended in 30 ml PBS with 1 % (final concentration) myristate and gently shaken at 37 °C for 30 min. Samples were centrifuged at 17,000 × g for 20 min at 4 °C. The pellet fraction was resuspended in 5 ml of sucrose solution (0.5 M sucrose, 0.15 M Tris [pH 8.0]). Following addition of lysozyme (0.1 mg/ml) and disodium EDTA (2 mM, pH 8.0), the suspension was stirred on ice for 30 min and then at room temperature for 20 min. Myristate was added to final concentration of 1 %, and the preparation was stirred at room temperature for 30 min. Samples were centrifuged at 17,000 × g for 10 min at 4 °C. Polyethylene glycol (2 %) was added to the supernatant, which was then incubated on ice for 30 min. The mixture was centrifuged at 27,000 × g for 20 min at 4 °C. The pellets were washed in 10 ml of water and centrifuged at 80,000 × g for 30 min at 4 °C. Finally, the PFs were resuspended in 1.0 ml water and stored at 4 °C.

Dark-field microscopy. Live *B. burgdorferi* cells were observed under a dark-field microscope (Zeiss Axio Imager. M1) connected to an AxioCam digital camera. Exponentially growing cells were mixed with 1.0 methylcellulose (400 mesh, Sigma-Aldrich) and video recorded at room temperature (23 ºC). All the mutants in this study (Δ*fliE*, Δ*flgB*, Δ*flgBC*, Δ*flgC*, Δ*flhO*, Δ*flgG*, Δ*flgE*, and *flaB*) are rod-shaped and non-motile, while the WT cells and the complemented strain Δ$flgE^{com}$ show the flat-wave morphology (Fig. S9).

Frozen-hydrated sample preparation. Frozen-hydrated specimens were prepared as described previously (8). Briefly, the *B. burgdorferi* culture was centrifuged at 5,000 × g for 5 min and the resulting pellet were rinsed gently with 1.0 ml PBS. The cells were centrifuged again and were finally suspended in 30~50 µl PBS. The cultures were mixed with 10 nm (or 15 nm) colloidal fiducial gold markers and were then deposited onto freshly glow-discharged, holey carbon grids for 1 min. Grids were blotted with filter paper and then rapidly frozen in liquid ethane, using a homemade gravity-driven plunger apparatus.

Cryo-electron tomography. Frozen-hydrated specimens were imaged at -170 °C using a Polara G2 electron microscope (FEI) equipped with a field emission gun and a 16 megapixel CCD camera (TVIPS). The microscope was operated at 300 kV with a magnification of 31,000 ×, resulting in an effective pixel size of 5.7 Å after 2x2 binning. Using the FEI "batch tomography" program, low-dose, single-axis tilt series were collected from each cell at -6 to -8 µm defocus with a cumulative dose of ~100 $e^-/Å^2$ distributed over 87 images and covering an angular range of -64° to +64°, with an angular increment of 1.5°. Tilt series were automatically aligned and reconstructed using a combination of IMOD (9) and RAPTOR (10). In total, 234,552 images and 2,696 tomographic reconstructions were generated and used for further processing (Table S2).

Sub-volume averages, correspondence and classification analyses. Conventional imaging analysis, including 4×4×4 binning, contrast inversion, and low-pass filtering enhanced the contrast of binned tomograms (11). The subvolumes (256×256×256 voxels) of the flagellar motors were extracted computationally from the tomograms and were further aligned as previously described (8, 12). A total of 15,380 flagellar motor subvolumes were manually selected from 2,696 reconstructions (Table S2).

The initial orientation of each particle was estimated by the center of the collar and the center of the C ring, thereby providing two of the three Euler angles. To accelerate image analysis, 4×4×4 binned subvolumes (64×64×64 voxels) were used for initial alignment. A global average of all the extracted 4×4×4 binned subvolumes was performed after application of the two Euler angles previously determined. After an initial alignment that was based on the global average, multivariate statistical analysis and hierarchical ascendant classification were applied to analyze the subvolumes of the motor in each mutant. Then, 2×2×2 binned subvolumes (128×128×128 voxels) and original subvolumes (256×256×256 voxels) were subsequently utilized for further image analysis and refinement. Class averages were computed in Fourier space, so the missing wedge problem (11, 13) of tomography was minimized. Fourier shell correlation coefficients with a threshold of 0.5 were estimated by comparing the correlation between two randomly divided halves of the aligned images used to generate the final maps (Table S2).

3-D visualization. Surface rendering of 3-D flagellar structures were carried out using the software package UCSF Chimera (14). 3-D segmentations of reconstructions from a wild type cell and a Δ*fliE* cell were constructed manually using the 3-D modeling software Amira (Visage Imaging). The filaments, the outer and inner membranes, and the peptidoglycan layer were manually segmented (Movie S1, S2). The isosurface maps from the flagellar motor were computationally mapped back into the original cellular context.

Supplementary Figures

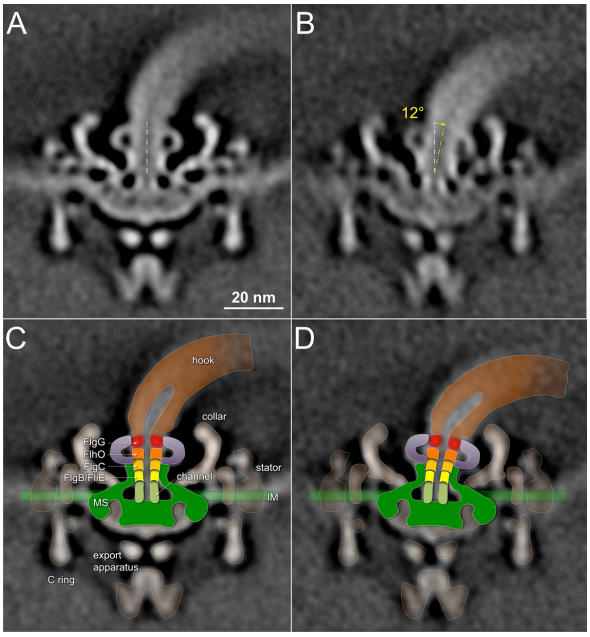

Fig. S1. Classification of flagellar motors from wild type cells reveals two distinct conformations of the rod. (A) Central section of an asymmetric reconstruction of the intact flagellar motor with a straight rod. (B) Central section of an asymmetric reconstruction of the intact flagellar motor with a tilted rod. The titled angle is ~12° comparing the straight rod in (A). (C-D) The cartoon models of the MS ring, the modular rod and the hook overlay on cryo-ET maps in (A-B).

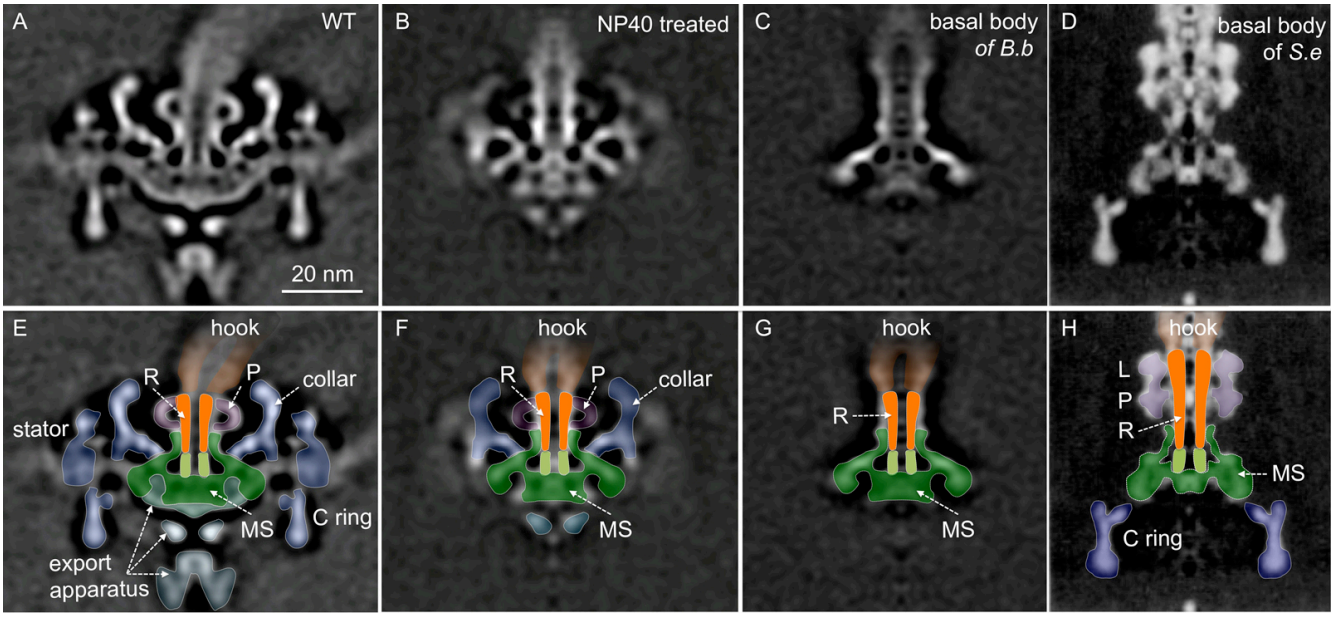

Fig. S2. Comparing the flagellar basal bodies of *B. burgdorferi* and *S. enterica*. (A) The intact flagellar motor of *B. burgdorferi*. (B) Detergent (Nonidet P-40) treated flagellar motor of *B. burgdorferi* (8). In this map, the C ring, stator, and a portion of the export apparatus are removed by the detergent treatment. The densities of periplasmic structures (i.e. the P ring and collar) become weaker than those of wild type. (C) Purified flagellar basal body of *B. burgdorferi*. In this map, most of the periplasmic structures, membrane and its integrated structures, and cytoplasmic structures are dissolved during the purification. The remained basal body is believed to be the MS ring and rod complex. (D) The basal body of *S. enterica* reported by Francis *et al* (15). (E-H) Density outline of the EM maps (A-D). The MS is outlined in green. The channel domain in the MS ring that connects the rod is colored in light green. Rod is outlined in orange color. Notably, the MS ring and rod complex have a similar contour in the two types of flagellar motors, as shown in (E-H). The other densities are assigned to be the C ring, the collar, the stator, the P-ring, L-ring, and the hook, as outlined in each EM map. The scale bar is 20 nm.

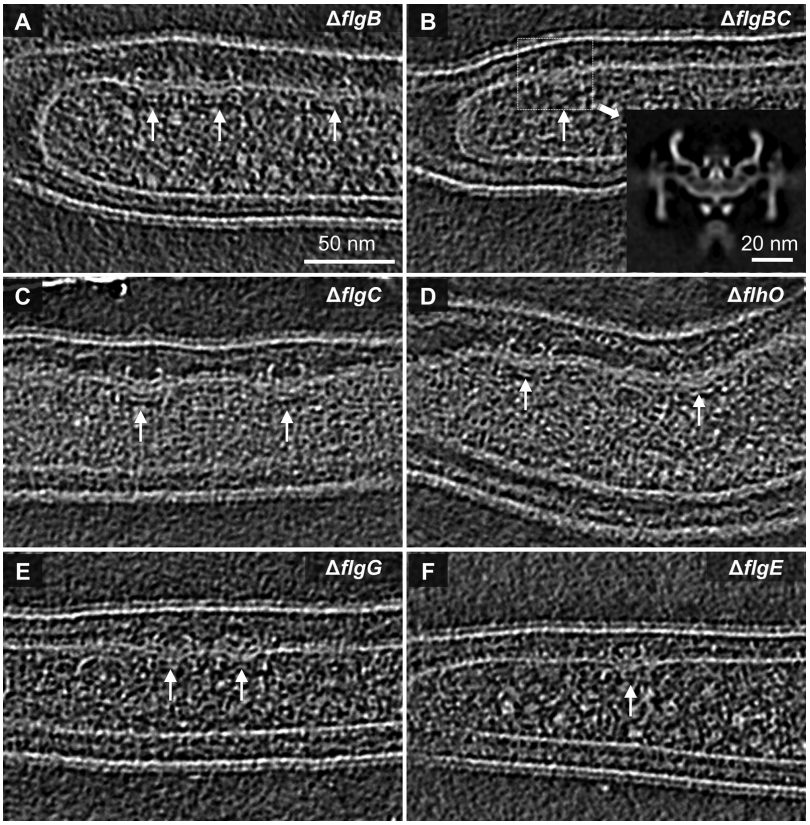

Fig. S3. Cryo-tomograms of Δ*flgB*, Δ*flgBC*, Δ*flgC*, Δ*flghO*, Δ*flgG*, Δ*flgE*. (A) Cryo-ET section of Δ*flgB* cell. (B) Cryo-ET section of Δ*flgBC* cell. The 3-D averaged structure of Δ*flgBC* flagellar motor was shown in the inset panel. The flagellar motor is reconstructed by averaging 714 Δ*flgBC* flagellar motors. The channel domain of the MS ring is a closed conformation as that observed in Δ*flgB* mutant, indicating the assembly order of FlgB is earlier than FlgC. (C) Cryo-ET section of Δ*flgC* cell. (D) Cryo-ET section of Δ*flhO* cell. (E) Cryo-ET section of Δ*flgG* cell. (F) Cryo-ET section of Δ*flgE* cell. The scale bar is 50 nm for each tomogram. The flagellar motors locate beneath the PG layer, as indicated by arrows.

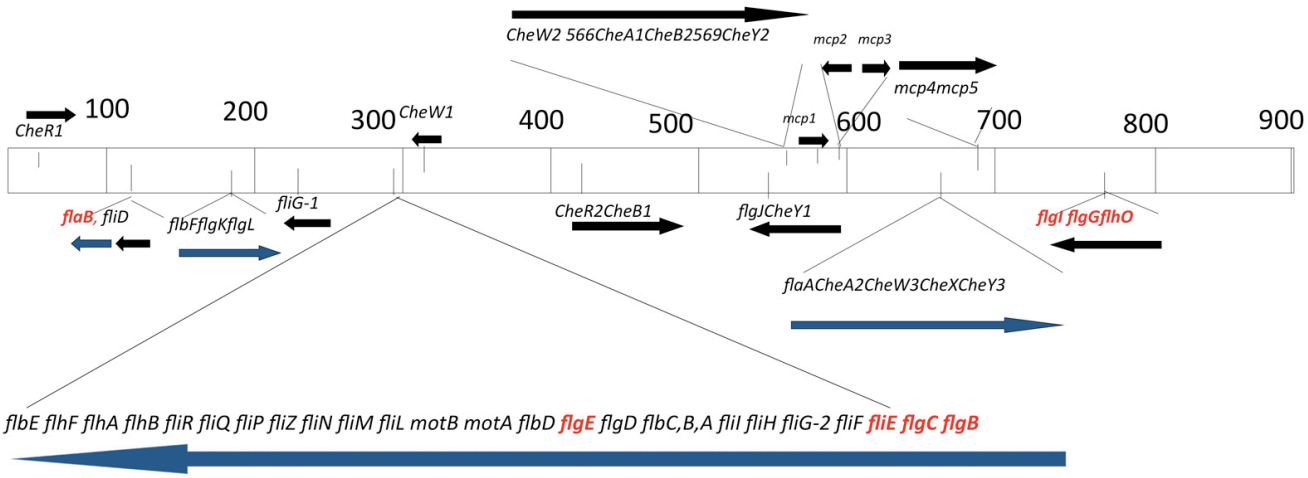

Fig. S4. Organization of the motility and the chemotaxis genes in *B. burgdorferi* (16)**.** Black arrows indicate direction of transcription of genes, and promoters have been identified by primer extension and operons by RT-PCR (2, 17). Blue arrows indicate presumed promoters, operons, and direction of transcription based solely from sequence analysis. The genes inactivated in this study are highlighted in red color.

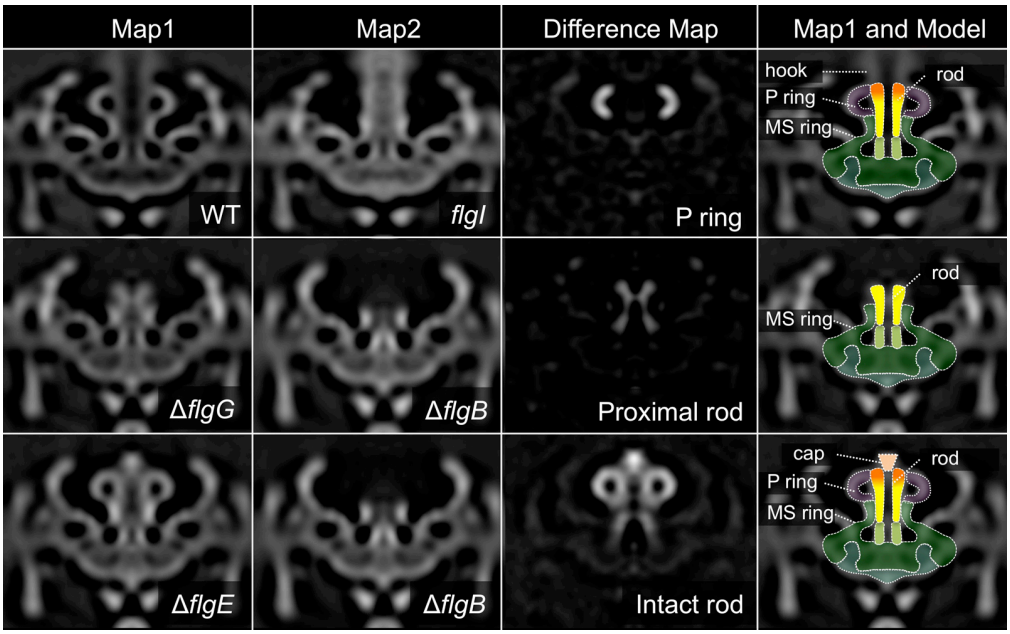

Fig. S5. Difference maps are required to define the structures of the P ring and the rod. Central sections of the motor structures from WT, Δ*flgG*, and Δ*flgE* are shown in the first column, respectively. Central sections of the motor structures from Δ*flgB* and *flgI* are shown in the second column, respectively. The difference maps between those from the first and second columns are shown in the third column, respectively. Cartoon models are overlaid on the maps in the fourth column.

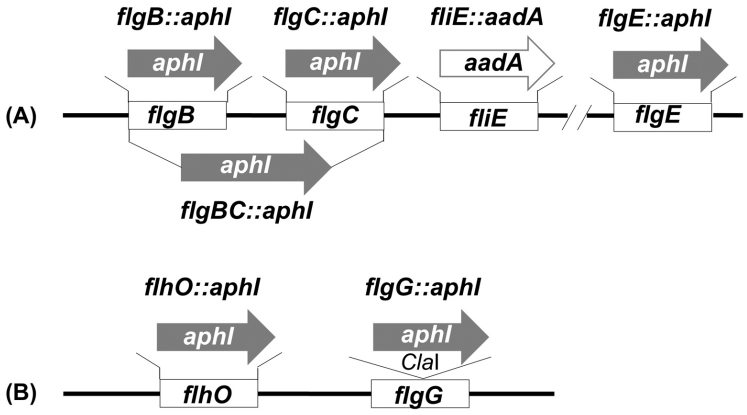

Fig. S6. Diagrams illustrating construction of vectors for the targeted mutagenesis of *flgB*, *flgC*, *flgBC*, *fliE*, *flgE*, *flhO*, and *flgG* genes in *B. burgdorferi*. For the vectors of *flgB::aphI*, *flgC::aphI*, *fliE::aadA*, and *flhO::aphI*, the entire genes are *in-frame* deleted and replaced by either a*phI* or *aadA* cassettes; for *flgBC::aphI*, both the *flgB* and *flgC* genes are *in-frame* deleted and replaced by *aphI*; and for *flgG::aphI*, the *flgG* gene is inactivated by directly inserting the *aphI* cassette at a ClaI cut site.

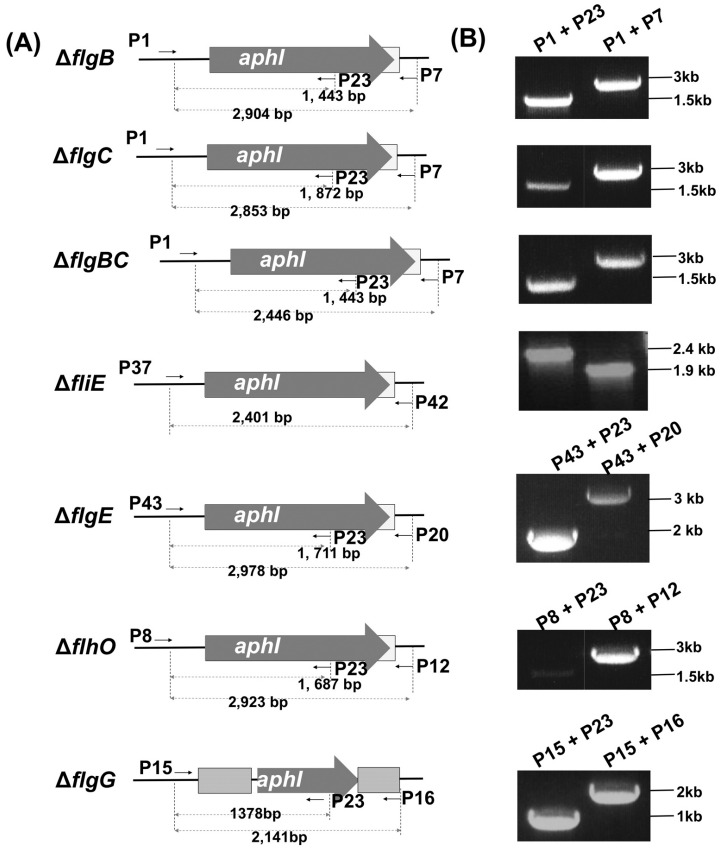

Fig. S7. Characterization of flagellar rod mutants of *B. burgdorferi* by PCR. (A) A diagram illustrating how the PCR analysis was designed. As illustrated, primer P1, P37, P43, P8, and P15 are located at the flanking regions of the constructs for the targeted mutagenesis; primer P23 is located within the *aphI* cassette; and primer P7, P42, P20, P12, and P16 are located at the 3' end of the constructs. Arrows represent the relative positions and orientations of these primers; the numbers are predicted sizes of PCR products generated by the corresponding primers. The sequences of these primers are listed in Table S5. (B) PCR analysis of the seven mutants. Two pairs of primers were used for each mutant. The numbers are approximate sizes of detected PCR products generated by the corresponding primers as labeled.

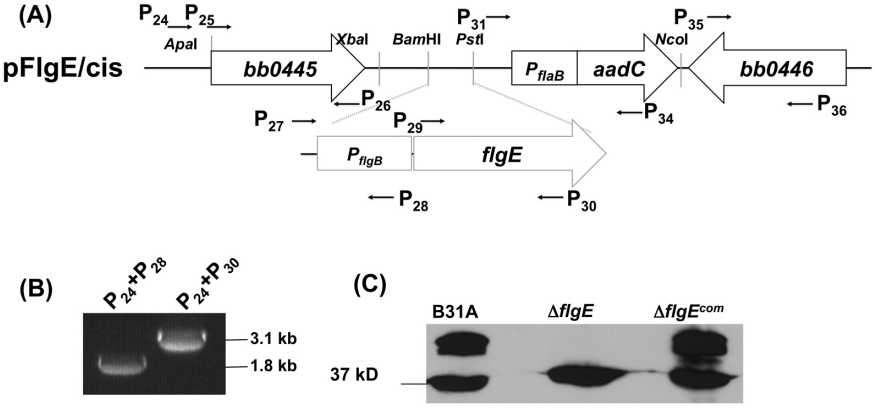

Fig. S8. Constructing a *cis*-complemented Δ*flgE* mutant, Δ*flgE*^{com}. (A) Diagrams illustrating how the Δf*lgE*^{com} strain is constructed. To construct pFlgE/cis, the *flgB* promoter (P_{flgB}) was PCR amplified and fused to the 5' end of *flgE*. The obtained fragment was then inserted into the pCisCom construct at the BamHI cut site, yielding pFlgE/cis. (B) PCR analysis of Δ*flgE*^{com}. Two pairs of primers were used for PCR amplifications and the obtained PCR products were visualized by DNA electrophoresis. The numbers are approximate sizes of detected PCR products generated by the corresponding primers as labeled. (C) Immunoblotting analysis of the whole-cell lysate of the WT, Δ*flgE*, and Δ*flgE*^{com} strains probed with a specific antibody against FlgE.

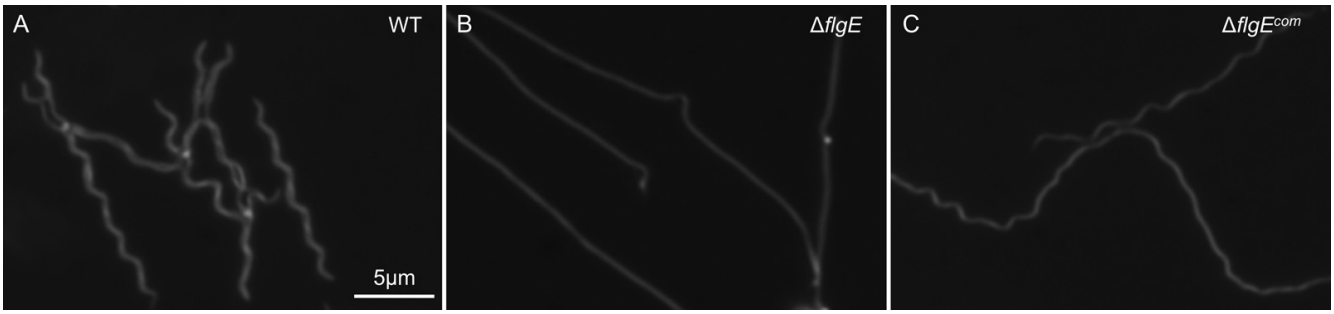

Fig. S9. Cell morphology of wild type (WT), Δ*flgE*, and its complemented strain Δ*flgE*^{com}. (A) WT cell shows the flat-wave morphology of *B. burgdorferi*. (B) Δ*flgE* mutant cells are rod-shaped. All the mutants in this study (Δ*fliE*, Δ*flgB*, Δ*flgBC*, Δ*flgC*, Δ*flhO*, Δ*flgG*, Δ*flgE*, and *flaB*) have similar rod-shaped morphology as Δ*flgE*. (C) The complemented strain restores the flat-wave morphology.

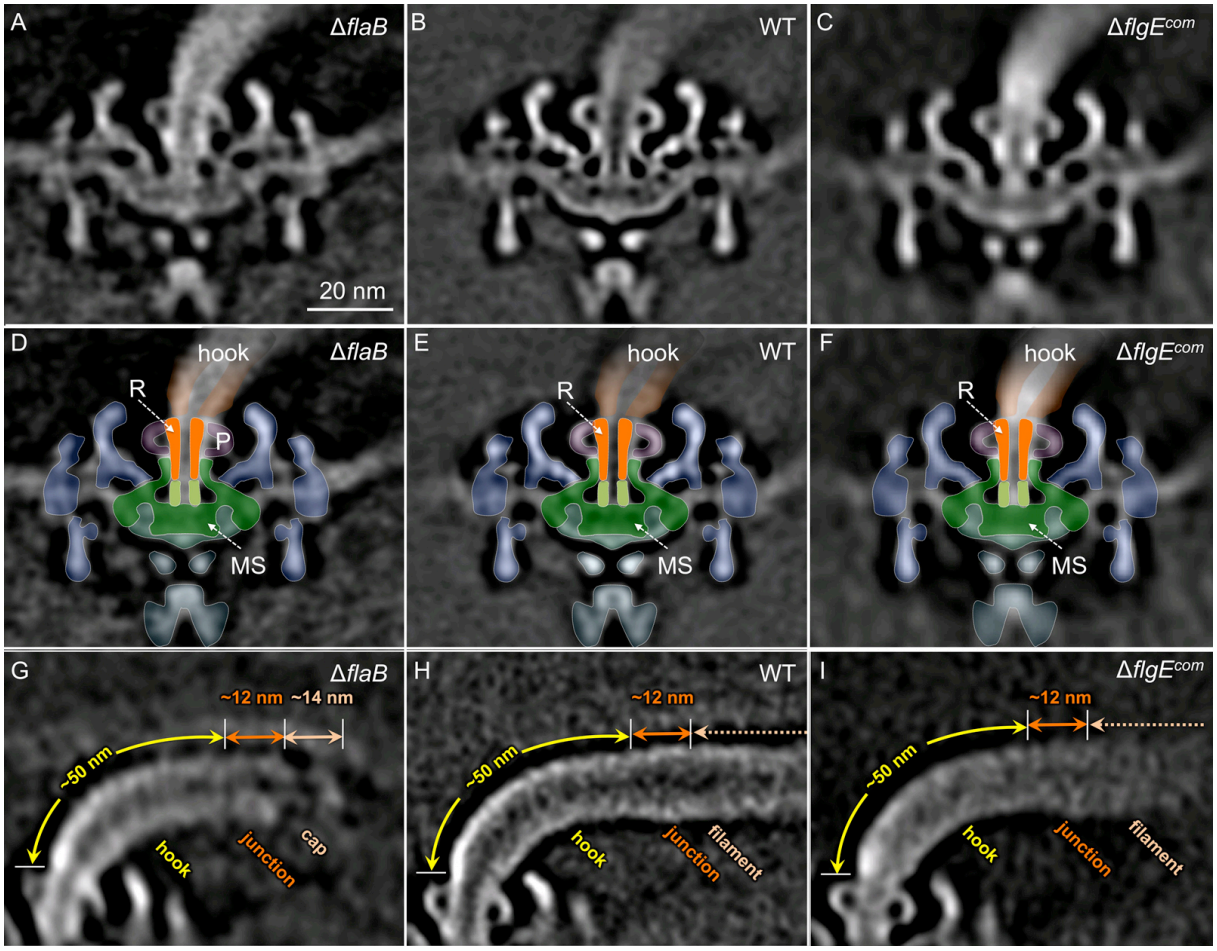

Fig. S10. Comparison of the reconstructions of flagellar motors from *flaB*, wild type, and Δ*flgE* complemented strain. (A) Central section of an asymmetric reconstruction of *flaB* flagellar motor. The flagellar motor structure is reconstructed by averaging 551 subvolumes. (B) Central section of an asymmetric reconstruction of the wild type flagellar motor, which is also shown in Fig. 1E. (C) Central section of an asymmetric reconstruction of the flagellar motor in Δ*flgE*^{com}, a complemented Δ*flgE* strain. The flagellar motor structure is reconstructed by averaging 571 subvolumes. (D-F) The cartoon models of the MS ring, the rod (R) and the hook overlay on cryo-ET maps in (A-C). The flagellar motor architectures of *flaB* and Δ*flgE*^{com} are identical to that in wild type. (G) The reconstruction of the flagellar hook in the *flaB* mutant, as illustrated in Fig. 5B. (H) The reconstruction of the wild type flagellar hook-filament, as illustrated in Fig. 5F. (I) The reconstruction of flagellar hook-filament in Δ*flgE*^{com} by local alignment of the axial region.

Supplementary Tables

Table S1. Strains used in this study

B. burgdorferi Samples	Gene	Role and Function	Morphology	Motility	Reference
Wild type	N/A	N/A	flat-wave	motile	Liu *et al*. (2009)
Basal body	N/A	N/A	N/A	N/A	Sal *et al*. (2008)
Δ*fliE*	BB0292	MS ring rod junction	rod-shaped	nonmotile	This study
Δ*flgB*	BB0294	proximal rod protein	rod-shaped	nonmotile	This study
Δ*flgC*	BB0293	proximal rod protein	rod-shaped	nonmotile	This study
Δ*flgBC*	BB0293/ BB0294	proximal rod protein	rod-shaped	nonmotile	This study
Δ*flhO*	BB0775	proximal rod protein	rod-shaped	nonmotile	This study
Δ*flgG*	BB0774	distal rod protein	rod-shaped	nonmotile	This study
Δ*flgE*	BB0283	hook protein	rod-shaped	nonmotile	This study
flaB	BB0147	filament protein	rod-shaped	nonmotile	Motaleb *et al*. (2000)
Δ*flgE*^{com}	N/A	N/A	flat-wave	motile	This study

Table S2. Cryo-ET data and parameters used in this study

Samples	Cryo tomograms	CCD images	Subvolumes of motor	Nominal Defocus (μm)	Mag (x1000)	Pixel size (nm)	Resolution (FCS=0.5) (nm)
Wild type	1,266	110,142	7,047	-6	31	0.57	3.5
Basal body	143	12,441	286	-8	31	0.57	5.1
Δ*fliE*	218	18,531	1,083	-8	31	0.57	3.9
Δ*flgB*	136	11,832	1,096	-8	31	0.57	3.9
Δ*flgC*	245	21,315	916	-8	31	0.57	3.8
Δ*flgBC*	102	8,874	714	-6.8	31	0.57	N/A
Δ*flhO*	149	12,963	1,304	-8	31	0.57	3.9
Δ*flgG*	95	8,265	622	-8	31	0.57	3.7
Δ*flgE*	113	9,831	716	-8	31	0.57	3.8
flaB	62	4,030	551	-9	23	0.76	4.8
Δ*flgE*^{COM}	79	5,135	571	-8	23	0.76	N/A

Table S3. Sequence alignment of flagellar rod-hook-filament substrates

		fliE *bb0292*	*flgB* *bb0294*	*flgC* *bb0293*	*flhO* *bb0775*	*flgG* *bb0774*	*flgD* *bb0284*	*flgE* *bb0283*	*flgK* *bb0181*	*flgL* *bb0182*	*fliD* *bb0149*	*flaB* *bb0147*	*flgI* *bb0772*
B.b Vs. S.e	identity	23%	27%	37%	29%	50%	32%	32%	24%	24%	23%	25%	17%
	similarity	52%	46%	59%	42%	68%	53%	47%	42%	46%	41%	24%	37%

```
FliE_S.e_        ----MAAIQGIEGVISQLQATAMAARGQDTHSQSTVSFAG--QLHAALDRISDRQAAARV 54
FlgB_S.e_        MLDRLDAALRFQQEALNLRAQRQEILAANIANADTPGYQA---RDIDFASEL-KKVMVRG 56
FlgC_S.e_        --MALLNIFDIAGSALAAQSKRLNVAASNLANADSVTGPD----GQPYRAKQ-VVFQVDA 53
FlgF_S.e_        ----MDHAIYTAMGAASQTLNQQAVTASNLANASTPGFRA---QLNALRAVP-VDGLSLA 52
FlgG_S.e_        ----MISSLWIAKTGLDAQQTNMDVIANNLANVSTNGFKR---QRAVFEDLL-YQTIRQP 52
FliE_B.b_        ---MVRTDAFFTENNINLVKKNPLHFDVNLFSSKSNAKDN---DIKTFKDVL-INSITDV 53
FlgB_B.b_        -MNDFERSVDFSHRYLDVLSLRQSVISDNIANIDTPNFKR---SKISFESEL-EKAFLNE 55
FlgC_B.b_        --MGLFSSINVASTGLTAQRLRIDVISNNIANVSTSRTPD----GGPYRRQR-IIFAPRV 53
FlhO_B.b_        ----MVRGIYTAASGMMAERRKLDTVSNNLANIDLIGYKKDLSIQKAFPEML-IRRLNDD 55
FlgG_B.b_        ----MMRALWTAASGMTAQQYNVDTIANNLSNVNTTGFKK---IRAEFEDLI-YQTHNRA 52
                     .                          :  . .

FliE_S.e_         ----LGEPGIALNDVMADMQKASVSMQMGIQVRNKLVAAYQEVMSMQV-- 104
FlgB_S.e_         ----LDGNTVDMDRERTQFADNSLKYQMGLTVLGSQLKGMMNVLQGGN-- 138
FlgC_S.e_         ---YVKMPNVDVVGEMVNTMSASRSYQANIEVLNTVKSMMLKTLTLGQ-- 134
FlgF_S.e_        MSGVLEGSNVKPVEAMTDMIANARRFEMQMKVITSVDENEGRANQLLSMS 251
FlgG_S.e_        YQGYVETSNVNVAEELVNMIQVQRAYEINSKAVSTTDQMLQKLTQL---- 260
FliE_B.b_        ------PSSIDVHDVVIAMSKANMNLSILKAVVERGVKAYQDIINIR--- 111
FlgB_B.b_        ----NNGNNVDIDSEVKALVQNQMMYHLMTNVQAHYFKSINIVLK----- 135
FlgC_B.b_        ---YVELPNVNLVEEMVDMISASRAYEANSTVINSSKSMFRSALAILQG- 152
FlhO_B.b_        ETETLEASNVNAVKEMVLMIEINRAYEANQKTIQTEDSLLGKLINEIGKY 282
FlgG_B.b_        RQGILEMSNVSIAEEMVTMIVAQRAYEINSKAIQTSDNMLGIANNLKRQ- 265
                                .
```

* The heptad hydrophobic amino acids are highlighted.

Table S4. FliF sequence alignment

```
Helicobacter_pylori      EERITLASQGIPKTSKVGFEIFDTKDFGATDFDQNIKLIRAIEGELSRTI 146
Campylocbacter_jejuni    RQRMFIASEGLIKDSRVGFEAFDTQAFGATNEEQKVKYQRAIEGELARTI 145
Samonella_enterica       ELRLRLAQQGLPKGGAVGFELLDQEKFGISQFSEQVNYQRALEGELARTI 144
Escherichia_coli         ELRLRLAQQGLPKGGAVGFELLDQEKFGISQFSEQVNYQRALEGELSRTI 141
Borrelia_burgdoferi      KMRAILVREELVPVHMDPWALFDIDRWTITDFERSINLRRSITRAVEQHI 145
Treponema_pallidium      RMRSILIREDLIPKNVDPWAIFDVERWTRTDFERRVDVRRAINNTVTNHI 145
                         . *  :  : :       :  :* . :  :: .. :.  *::   : . *

Helicobacter_pylori      ESLNPILKANVHIAIPKDSVFVAKEVPPSASVMLKLKPDMKLS--PTQIL 194
Campylocbacter_jejuni    ETLEPIRSAVVHIAFPKDSVFTERQIPPTASVVVNVREGLKLT--RKQID 193
Samonella_enterica       ETLGPVKSARVHLAMPKPSLFVREQKSPSASVTVTLEPGRALD--EGQIS 192
Escherichia_coli         ETIGPVKGARVHLAMPKPSLFVREQKSPSASVTVNLLPGRALD--EGQIS 189
Borrelia_burgdoferi      VALDDVDAVSVNLVMPEKALFKESQEPVKASVRITPRPGSDIITNRKKVE 195
Treponema_pallidium      KALDDIDDAHVVINVPEDALFQADQKPITASVVIFPKPSSTIASERKKIE 195
                          ::  :  . * : .*: ::*   : . .*** :    .  :     ::

Helicobacter_pylori      GIKNLIAAAVPKLTIENVKIVNENGESIGEGDILENSK--ELALEQLHYK 242
Campylocbacter_jejuni    GIKNIVSAAVPKLTKENVKISDQSGVPLDEQEAYED----DLVRAQIKFK 239
Samonella_enterica       AVVHLVSSAVAGLPPGNVTLVDQSGHLLTQSNTSGR----DLNDAQLKFA 238
Escherichia_coli         AIVHLVSSAVAGLPPGNVTLVDQGGHLLTQSNTSGR----DLNDAQLKYA 235
Borrelia_burgdoferi      GLVKLIQYAIEGLESDNIAIVDNSGTILNDFSNLDGIDRIDLAEKERKLK 245
Treponema_pallidium      GIQKLLKLAVPGLKDENITIVDSDATVLNDFEGFKDADRLSLIEKQQKMI 245
                         .: :::  *:  *   *: : :...  : : .        .*   : :
```

* The heptad hydrophobic amino acids are highlighted in a segment of FliF sequence (130~230).

Table S5. Oligonucleotide primers used to construct rod mutant plasmid.

Primers	Sequence (5'-3')	Note
P1	AGGGATCTAGTAATTCTGAG	*flgB* flanking region; [F]
P2	CGGGTGGTAATTTTGAAGAG	*flgB, flgC, flgBC* inactivation;[F]
P3	ACGTTTCCCGTTGAATATGGCTCA TATTGAAACCTCCCTCATT	*flgB, flgBC* inactivation; [R]
P4	TTTGATGCTCGATGAGTTTTTCTAA ATTAATATCTTAAGGAATGT	*flgB* inactivation; [F]
P5	ACGTTTCCCGTTGAATATGGCTCA TTTTACATTCCTTAAGATATT	*flgC* inactivation; [R]
P6	TTTGATGCTCGATGAGTTTTTCTAA AGGAGAGATCATTGGTGAG	*flgC, flgBC* inactivation; [F]
P7	TCAAACAAAGCCCATGGATC	*flgB, flgC, flgBC* inactivation; [R]
P8	CTCTTCACTAAAAACCTCTC	*flhO* flanking region; [F]
P9	GGCGCTGGAACAAGATTATG	*flhO* inactivation; [F]
P10	ACGTTTCCCGTTGAATATGGCTCA TGGTTAAATCCTTAAAGAC	*flhO* inactivation; [R]
P11	TTTGATGCTCGATGAGTTTTTCTAA AATGAAATTGGAAAATATT	*flhO* inactivation; [F]
P12	TGTTTTACTAGGCGCAATGT	*flhO* inactivation; [R]
P13	TTATGGACAGCAGCAAGTG	*flgG* inactivation; [F]
P14	CAATTCCTAACATATTGTC	*flgG* inactivation; [R]
P15	ATGAGAGCATTATGGACAG	*flgG* flanking region; [F]
P16	TTGCCTTTTTAAGTTATTTG	*flgG* flanking region; [R]
P17	GGATCCTGTTGATAGGTATAAAGT	*flgE* inactivation; [F]
P18	ACGTTTCCCGTTGAATATGGCTCA TATAATTATTCCTCCAAAC	*flgE* inactivation; [R]
P19	TTTGATGCTCGATGAGTTTTTCTAA TCTAAGATTGTTTTTTTAGT	*flgE* inactivation; [F]
P20	CTCGAGTTCACCACCAATGCTACT	*flgE* inactivation; [R]
P21	ATCGATTAATACCCGAGCTTCAAG	*aphI*, *flgG* inactivation; [F]
P22	ATCGATTCAAGTCAGCGTAATCTCTC	*aphI*, *flgG* inactivation; [R]
P23	GACTGAATCCGGTGAGAATG	*aphI*; [R]
P24	ACTGGACACGCAACTAAACT	*bb0445* flanking region; [F]
P25	GGGCCCGGAGTGATATAAATGGGTGT	*bb0445* region; [F]
P26	GGATCCTCTAGAGCTCAAAAAGCAGCTT	*bb0445* region; [R]
P27	GGATCCTACCCGAGCTTCAAGGAAG	*flgB* promoter; [F]
P28	CATATGATGGAAACCTCCCTCATT	*flgB* promoter; [R]
P29	CATATGATGAGGTCTTTATATTC	*flgE;*[F]
P30	GGATCCTTAATTTTTCAATCTTACAAG	*flgE;*[R]
P31	CTGCAGGTACCTGTCTGTCGCCTCTTGTG	*flaB* promoter; [F]
P32	CATATGTCATTCCTCCATGATAAAAT	*flaB* promoter; [R]
P33	CATATGTTACGCAGCAGCAACGA	*accC1*; [F]
P34	GAGCTCCATGGTTAGGTGGCGGTACTTGGGT	*accC1;* [R]
P35	GAGCTCATGGCAGAGCTTGCATTATG	*bb0446*; [F]
P36	ATGCATCTACCTCAATCTCCACAACT	*bb0446*; [R]
P37	GCCCAGGAGGTCCCCAGGG	*fliE* inactivation; [F]
P38	CAAGGTAGTCGGCAAATAAGGAGCCATAAGATTTTGAG	*fliE* inactivation; [R]
P39	CTCAAAATCTTATGGCTCCTTATTTGCCGACTACCTTG	*aadA, fliE* inactivation; [F]
P40	CAAGGCTAAAGGAGAGATCAATGAG GGAAGCGGTGATCG	*aadA, fliE* inactivation; R]
P41	CGATCACCGCTTCCCTCATTGATCTCT CCTTTAGCCTTG	*fliE* inactivation; [F]
P42	GATTCTGAGGTTAAGGCAC	*fliE* inactivation; [R]
P43	TTTAACTGCTTTGATTGATG	*flgE* upstream flanking region; [F]

[a] Underlined sequences are engineered restriction cut sites for DNA cloning; [F] forward; [R] reverse.

Supplementary References

1. Zhang K, Tong BA, Liu J, & Li C (2012) A single-domain FlgJ contributes to flagellar hook and filament formation in the Lyme disease spirochete Borrelia burgdorferi. *J Bacteriol* 194(4):866-874.
2. Ge Y & Charon NW (1997) Identification of a large motility operon in Borrelia burgdorferi by semi-random PCR chromosome walking. *Gene* 189(2):195-201.
3. Motaleb MA, Pitzer JE, Sultan SZ, & Liu J (2011) A novel gene inactivation system reveals altered periplasmic flagellar orientation in a Borrelia burgdorferi fliL mutant. *J Bacteriol* 193(13):3324-3331.
4. Motaleb MA*, et al.* (2000) Borrelia burgdorferi periplasmic flagella have both skeletal and motility functions. *Proc Natl Acad Sci U S A* 97(20):10899-10904.
5. Motaleb MA, Miller MR, Bakker RG, Li C, & Charon NW (2007) Isolation and characterization of chemotaxis mutants of the Lyme disease Spirochete Borrelia burgdorferi using allelic exchange mutagenesis, flow cytometry, and cell tracking. *Methods Enzymol* 422:421-437.
6. Sal MS*, et al.* (2008) Borrelia burgdorferi uniquely regulates its motility genes and has an intricate flagellar hook-basal body structure. *J Bacteriol* 190(6):1912-1921.
7. Li X*, et al.* (2007) The Lyme disease agent Borrelia burgdorferi requires BB0690, a Dps homologue, to persist within ticks. *Mol Microbiol* 63(3):694-710.
8. Liu J*, et al.* (2009) Intact flagellar motor of Borrelia burgdorferi revealed by cryo-electron tomography: evidence for stator ring curvature and rotor/C-ring assembly flexion. *J Bacteriol* 191(16):5026-5036.
9. Kremer JR, Mastronarde DN, & McIntosh JR (1996) Computer visualization of three-dimensional image data using IMOD. *J Struct Biol* 116(1):71-76.
10. Amat F*, et al.* (2008) Markov random field based automatic image alignment for electron tomography. *J Struct Biol* 161(3):260-275.
11. Liu J, Wright ER, & Winkler H (2010) 3D visualization of HIV virions by cryoelectron tomography. *Methods Enzymol* 483:267-290.
12. Liu J*, et al.* (2010) Cellular architecture of Treponema pallidum: novel flagellum, periplasmic cone, and cell envelope as revealed by cryo electron tomography. *J Mol Biol* 403(4):546-561.
13. Winkler H*, et al.* (2009) Tomographic subvolume alignment and subvolume classification applied to myosin V and SIV envelope spikes. *J Struct Biol* 165(2):64-77.
14. Pettersen EF*, et al.* (2004) UCSF Chimera--a visualization system for exploratory research and analysis. *J Comput Chem* 25(13):1605-1612.
15. Francis NR, Sosinsky GE, Thomas D, & DeRosier DJ (1994) Isolation, characterization and structure of bacterial flagellar motors containing the switch complex. *J Mol Biol* 235(4):1261-1270.
16. Li C, Motaleb A, Sal M, Goldstein SF, & Charon NW (2000) Spirochete periplasmic flagella and motility. *J Mol Microbiol Biotechnol* 2(4):345-354.
17. Ge Y & Charon NW (1997) Molecular characterization of a flagellar/chemotaxis operon in the spirochete Borrelia burgdorferi. *FEMS Microbiol Lett* 153(2):425-431.